ISSN (Print) 1226-1750
ISSN (Online) 2233-6656
Journal of Magnetics 28(2), 151-161 (2023) https://doi.org/10.4283/JMAG.2023.28.2.151

Impacts of Sr^{2+} and Annealing Temperature on the Composition, Structure, and Magnetic Properties of $SrFe_{12}O_{19}$ Synthesized by Tartrate Precursor Route

M. M. Hessien*, Mahdi Albogamy, Mohammed Alsawat, and Abdulrahman Alhadhrami

Department of Chemistry, College of Science, Taif University, P.O. Box 11099, Taif, 21944, Saudi Arabia

(Received 4 July 2021, Received in final form 3 April 2023, Accepted 4 April 2023)

Hexagonal M-type strontium ferrite ($SrFe_{12}O_{19}$) has been fabricated through a simple self-combustion tartrate precursor approach to producing a homogenous powder with a homogeneous shape and limited size distribution at low-processing temperatures. The impacts of the Sr^{2+}:Fe^{3+} molar ratio and the annealing temperature on formation, morphological structure, crystallite size, and magnetic performance were studied. The powders were characterized by scanning electron microscopy (SEM), X-ray diffraction (XRD) profile, and vibrating sample magnetometer (VSM). The development of crystalline single-phase Sr-hexagonal ferrite occurred at ≥ 1100 °C and Sr^{2+}:Fe^{3+} molar ratios 1.1:12-1.3:12. Existence of α-Fe_2O_3 and impurities in the hexagonal powders increases the lattice parameters while higher annealing temperature decreases it. The *c*/*a* ratios of as-prepared samples (~3.911-3.920) are comfortably within the range of ratios for M-type structures. The platelet-like structure has appeared at an annealing temperature ≥ 1000 °C. The wide saturation magnetization (37.26-66.19 emu/g) and coercivity (275.09-2107.8Oe) were accomplished at diverse synthesis conditions and reached the greatest values at 1350 °C. The squareness ratios (Mr/Ms) for all studied samples are <0.5, which is for multi-magnetic domains.

Keywords : Sr-hexaferrite, tartrate, precursor synthesis, molar ratio, morphology, magnetic property, annealing temperature.

1. Introduction

Ferrites are important technological materials that have both electrical and magnetic properties. Ferrites are now used in a diverse range of compositions, properties, and applications across many communication and electronic engineering fields [1-4] due to their large resistivity and lower raw material cost. Ferrite can be classified into four groups depending on crystal structure [5, 6]. They are hexagonal ferrite, garnet ferrite, spinel ferrite, and orthoferrites. The diversity of magnetic properties of these materials depends on their crystal structure because, in each case, it defines the interactions between the various ions on an atomic level.

Due to their characteristics and unique industrial and technological applications, hexagonal ferrites (hexaferrites) constitute a class of magnetic materials of utmost significance [7-10]. Hexaferrites (M, U, X, W, Y, and Z types) have gained considerable attention and intensive studies for many decades due to their excellent magnetic and functional properties [7, 11, 12]. Among them, M-type strontium hexagonal ferrites ($SrFe_{12}O_{19}$) and their derivative (substitutions) have been the subject of intensive study and interest due to their excellent functional properties [13-16]. Strontium hexaferrite has exemplary properties, including high coercive force, large saturation magnetization, excellent Curie temperature, excellent dielectric constant, high magnetocrystalline anisotropy, very large thermal and chemical stability, excellent dielectric constant, and nontoxicity along with simple accessibility [14, 17-19]. $SrFe_{12}O_{19}$ is widely used in practice as magnetic recording media, permanent magnets, and electromagnetic absorbing material [13-17]. Moreover, $SrFe_{12}O_{19}$ powders with a homogeneous structure and narrow size distribution are promising magnetic materials for industrial applications where they are ideal candidates for fabricating minipumps, actuators, micro-sized motors, and other devices [8, 20].

The magnetic properties of polycrystalline hexaferrite, which was prepared via the conventional ceramic route (solid-state reaction), entailing heating a stoichiometric

©The Korean Magnetics Society. All rights reserved.
*Corresponding author: Tel: +9665955235892
e-mail: m.hessien@tu.edu.sa

© 2023 Journal of Magnetics

mixture of iron oxide and strontium carbonate to a high temperature (≥ 1200 °C), were extremely low due to chemical inhomogeneity, large particle size, and introduction of impurities during ball milling [21-23]. The remanence (Mr) for the permanent magnet is a strong function of chemical composition, density, and orientation, while the coercivity (Hc) is related to microstructures. So, the target is to achieve a homogeneous structure with fine grain size and good chemical composition for excellent industrial applications by controlling the size distribution, crystalline size, and chemical compositions [24, 25]. Consequently, the improvement of magnetic properties can be monitored by controlling the synthesis strategies and the distribution of strontium and iron sites. Several soft synthetic routes were employed to synthesize strontium hexaferrite, including the hydrothermal method [28], coprecipitation [24, 27-29], and sol-gel method [30, 31], glass crystallization [32], self-propagating high-temperature synthesis method [33], mechanical alloying [34], and simple self-combustion tartrate precursor approach. For the synthesis of ferrite with single-phase powder, the tartrate precursor method is found to be more advantageous [12, 14, 35]. It is reported that this technique is an outstanding strategy for preparing ferrites with achievable compositional control microstructure, better homogeneity, uniform shape, and narrow size distribution with control morphology. These magnetic materials are suitable for microwave devices and the suppression of electromagnetic interference (EMI) [36].

The synthesis, structural, and magnetic properties of nanocrystalline Sr-hexaferrite powder by the chemical tartrate precursor method are examined in this article, along with the effects of the Sr^{2+}:Fe^{3+} molar ratio and annealing temperature. This method was chosen to create Sr-hexaferrite powder at a relatively low-processing temperature with a narrow size distribution, uniform shape, and homogenous microstructure. Effects of Sr^{2+}:Fe^{3+} molar ratios were also studied to show the optimum mole ratio that gives the single phase of strontium hexaferrite. Such research is crucial to understanding how to control the synthesis of Sr-hexaferrite in a single phase with the best magnetic properties. The Sr^{2+}:Fe^{3+} molar ratio was controlled from 1:12 to 1.3:12, while the annealing temperature was controlled from 900 to 1350 °C.

2. Experimental

2.1. Materials and Procedure

Strontium chloride hexahydrate, $SrCl_2 \cdot 6H_2O$ (RIEDEL-DE HAEN), iron (III) chloride anhydrous $FeCl_3$ (Sigma-Aldrich), lanthanum (III) nitrate hexahydrate, $La(NO_3)_3 \cdot 6H_2O$ (ACROS), and tartaric acid, $C_4H_6O_6$ (RIEDEL-DE HAEN), were used without any further purification. $C_4H_6O_6$ was used both as a chelating agent and as a fuel in the reaction system. As shown in Fig. 1, aqueous solutions of a precalculated amount of different Sr^{2+} and Fe^{3+} ions ratios based on chloride salts were prepared. Then, the tartaric acid was inserted into the various aqueous solutions. Table 1 records the four different series compositions. The total volume of the mixture was adjusted to 600 ml. The solutions were gently stirred at a temperature 90 °C to achieve good homogeneity until dryness. A sticky gel was formed thereafter and completely dried in the oven at 110 °C overnight to evaporate the liquid content and produce the gelling mass precursors. The dried precursors were then gently crushed, ground, and heated for two hours at a rate of 10 °C/min in a static air environment to the necessary annealing temperature (1000-1350 °C).

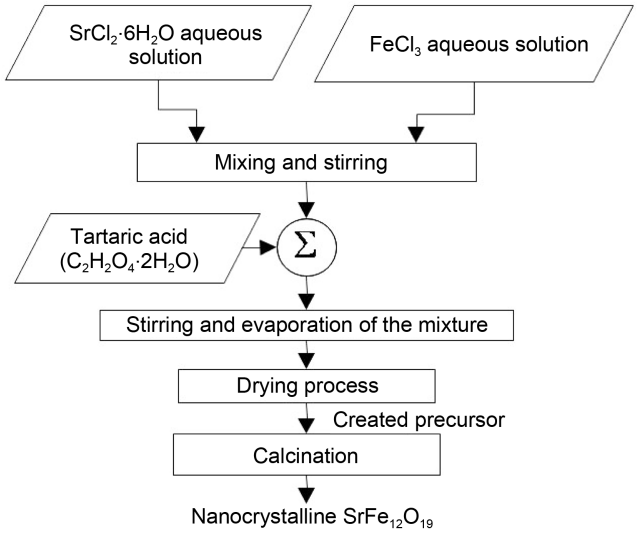

Fig. 1. Flow sheet diagram for the production of $SrFe_{12}O_{19}$ nanopowder by the tartaric acid precursor method.

2.2. Physical Properties

XRD profiles were distinguished by a model Bruker AXS diffractometer (D8-ADVANCE) with Cu Kα (λ = 1.54056 Å) radiation, operating at 40 kV and 10 mA to evaluate the phase evolution depending on the Joint Committee on Power Diffraction Standards (JCPDS) in the 2θ range from 20° to 75°. The average crystallite size (D_{xrd}) was estimated using the line broadening of the X-ray peaks by applying the well-known Debye-Scherrer equation [21]:

$$D_{xrd} = n\lambda/\beta\cos\theta, \quad (1)$$

Table 1. Precursor charges for the utilized chemical grades in mol (M) and gram (g).

Charge No.	Reactants		Product
	Charges in mol (M)	Charges in gram (g)	
1	1.0 M $SrCl_2{\cdot}6H_2O$ + 12 M $FeCl_3$ + 19 M $C_4H_6O_6$	$(\frac{266.62}{k})$g $SrCl_2{\cdot}6H_2O$ + $(\frac{1946.52}{k})$g $FeCl_3$ + $(\frac{2851.65}{k})$g $C_4H_6O_6$	$SrFe_{12}O_{19}$
2	1.1 M $SrCl_2{\cdot}6H_2O$ + 12 M $FeCl_3$ + 19 M $C_4H_6O_6$	$(\frac{293.282}{k})$g $SrCl_2{\cdot}6H_2O$ + $(\frac{1946.52}{k})$g $FeCl_3$ + $(\frac{2851.65}{k})$g $C_4H_6O_6$	$Sr_{1.1}Fe_{12}O_{19}$
3	1.2 M $SrCl_2{\cdot}6H_2O$ + 12 M $FeCl_3$ + 19 M $C_4H_6O_6$	$(\frac{319.944}{k})$g $SrCl_2{\cdot}6H_2O$ + $(\frac{1946.52}{k})$g $FeCl_3$ + $(\frac{2851.65}{k})$g $C_4H_6O_6$	$Sr_{1.2}Fe_{12}O_{19}$
4	1.3 M $SrCl_2{\cdot}6H_2O$ + 12 M $FeCl_3$ + 19 M $C_4H_6O_6$	$(\frac{346.61}{k})$g $SrCl_2{\cdot}6H_2O$ + $(\frac{1946.52}{k})$g $FeCl_3$ + $(\frac{2851.65}{k})$g $C_4H_6O_6$	$Sr_{1.3}Fe_{12}O_{19}$

k is an arbitrary scaling factor.

where λ is X-ray wavelength, θ is the Bragg angle, n is the Scherrer constant, and β is the full width at half maximum of the diffraction peak. The manipulation of all studied parameters (Sr^{2+}:Fe^{3+} molar ratio as well as the annealing temperature) on the lattice parameters characteristics of hexagonal ferrite particles was calculated based on the following equation [15]:

$$\frac{1}{d^2} = \frac{4}{3}\left(\frac{h^2 + k^2 + l^2}{a^2}\right) + \frac{l^2}{c^2}, \tag{2}$$

where h, k, and l are Miller indices and d is interplanar distance.

The unit cell volume (V) was defined with the values of a and c [15]:

$$V = \frac{\sqrt{3}}{2} a^2 c\,. \tag{3}$$

SEM was used to investigate the surface morphological structure and the average grain size. A VSM (7410-LakeShore, USA) was used to study the changes in the magnetic properties. Magnetic features were implemented at room temperature in a maximum applied field of 20 kOe.

3. Results and Discussion

3.1. X-Ray Diffraction Characterization

The impact of annealing temperature on the formation of the strontium hexaferrite ($SrFe_{12}O_{19}$) phase from the tartrate precursor was investigated through a series of experiments carried out at various annealing temperatures for 2 hours. Fig. 2 displays the XRD patterns of the formation of the strontium hexaferrite ($SrFe_{12}O_{19}$) phase from a tartrate precursor with a Sr^{2+}:Fe^{3+} molar ratio of 1:12 that was thermally treated at various temperatures (1000-1350 °C).

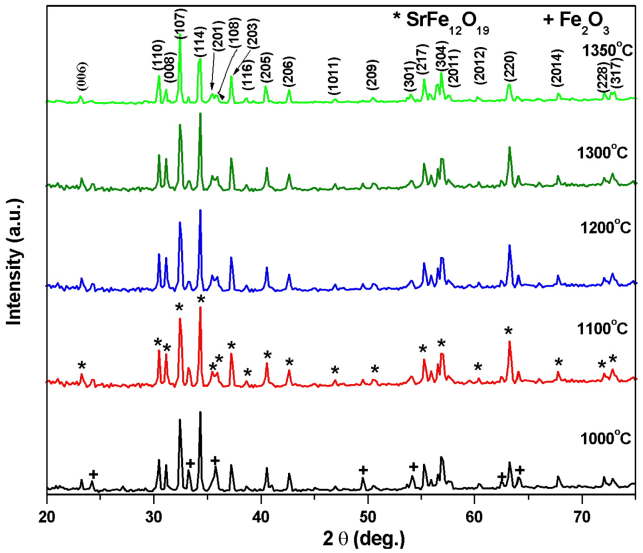

Fig. 2. (Color online) XRD patterns of $SrFe_{12}O_{19}$ for Sr^{2+}:Fe^{3+} molar ratio 1:12 treated at different temperatures.

The strongest diffraction planes (114), (107), (0 0 8) (110), (203), (2200), and (2011) of M-type hexagonal $SrFe_{12}O_{19}$ were differentiated by diffraction peaks at 2θ values of 34.17°, 32.31°, 31.085, 30.34°, 37.15°, 63.16° and 56.8°. A cubic form of α-Fe_2O_3 (JCPDS # 89-0599) was, however, achieved in each instance. The appearance of the -Fe_2O_3 phase was indicated by the diffraction patterns (104), (110), (116), (024), and (012) at 2θ values of 33.17°, 35.66°, 54.06°, 49.46°, and 24.14°, respectively. Fig. 3 elicits the phase progression with Sr^{2+} ion surplus (Fe/Sr content was 12:1.1) at various annealing temperatures. XRD patterns for the sample treated at 1000 °C consisted of crystalline hexagonal $SrFe_{12}O_{19}$ (JCPDS # 79-1412) and α-Fe_2O_3 (JCPDS # 89-0599) phases. The diffraction peaks at 2θ values of 33.17°, 35.66°, 54.06°, 49.46°, and 24.14° and the diffraction planes (104), (110), (116), (024), and (012) indicated the

presence of α-Fe_2O_3 phase impurities. On the other hand, the diffraction peaks at 2θ values of 30.34°, 31.085, 32.31°, 34.17°, 37.15°, 63.16°, and 56.8° corresponded to the strongest diffraction planes (110), (008), (107), (114), (203), (2200), and (2011). These patterns were attributed to the hexagonal Sr-M-hexaferrite $SrFe_{12}O_{19}$ phase. Moreover, the formation of $SrFe_{12}O_{19}$ hexaferrite somewhat increased when the calcination temperature rose to around 1100 degrees, as evidenced by the modest increase in peak intensities of the generated $SrFe_{12}O_{19}$ hexaferrite and the little increase in peak intensities of the free oxides. At the Sr^{2+}:Fe^{3+} mole ratio of 1:12, it is evident that the formation of single-phase strontium hexaferrite could not be obtained and contained secondary peaks of the α-Fe_2O_3 phase. Though, at this mole ratio and due to the limiting amount of Sr^{2+} ion in the dry precursor, the annealing temperature has a limiting effect on the formation of strontium hexaferrite. Although the annealing temperature significantly impacts the level of crystallinity, it has little bearing on the level of hexaferrite formation. This is due to hexagonal ferrite forming at a relatively lower calcination temperature. The tartrate precursor route is well known to be the most popular method for producing materials at a relatively lower calcination temperature than the conventional methods.

Fig. 3 demonstrates the diffraction profiles of the $SrFe_{12}O_{19}$ fabricated from a precursor with a Sr^{2+}:Fe^{3+} molar ratio of 1.1:12 at different temperatures (1000-1350 °C). At a low temperature of 1000 °C, the $SrFe_{12}O_{19}$ ferrite phase formed contained some impurity peaks due to the α-Fe_2O_3 phase. Meanwhile, at ≥ 1100 °C, a well-crystallized pure single $SrFe_{12}O_{19}$ phase was formed. The XRD patterns of $SrFe_{12}O_{19}$ from tartrate precursor with Sr^{2+}:Fe^{3+} molar ratios of 1.2:12 and 1.3:12 thermally treated at different temperatures for an annealing time of 2 h (Figs. 4, 5) show the same effect as Sr^{2+}:Fe^{3+} molar ratios 1.1:12, where a pure single phase of strontium hexaferrite was obtained at temperatures ≥ 1100 °C.

According to the XRD data and using the Debye-Scherrer formula, the crystallite size of the produced strontium hexaferrite phase for the most intense peak (107) was determined. Unsurprisingly, by raising the temperature from 1000 to 1350 °C for all Sr^{2+}:Fe^{3+} content,

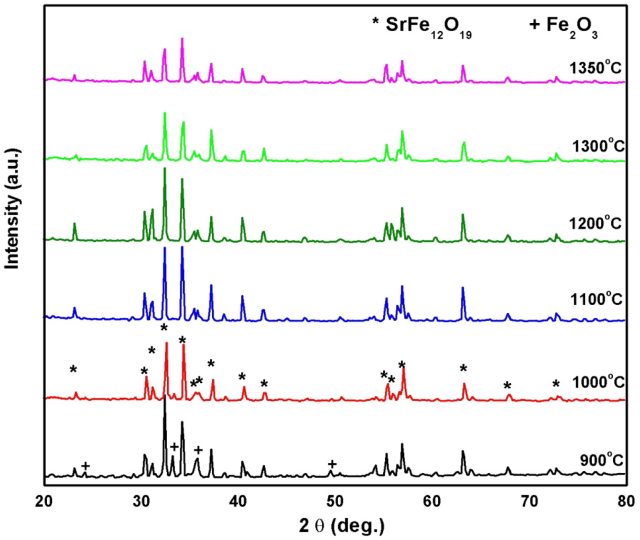

Fig. 4. (Color online) XRD patterns of $SrFe_{12}O_{19}$ for Sr^{2+}:Fe^{3+} molar ratio 1.2:12 treated at different temperatures.

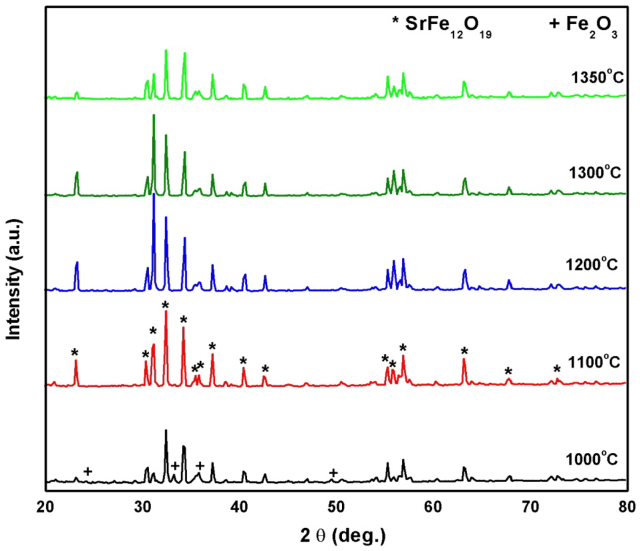

Fig. 3. (Color online) XRD patterns of $SrFe_{12}O_{19}$ for Sr^{2+}:Fe^{3+} molar ratio 1.1:12 treated at different temperatures.

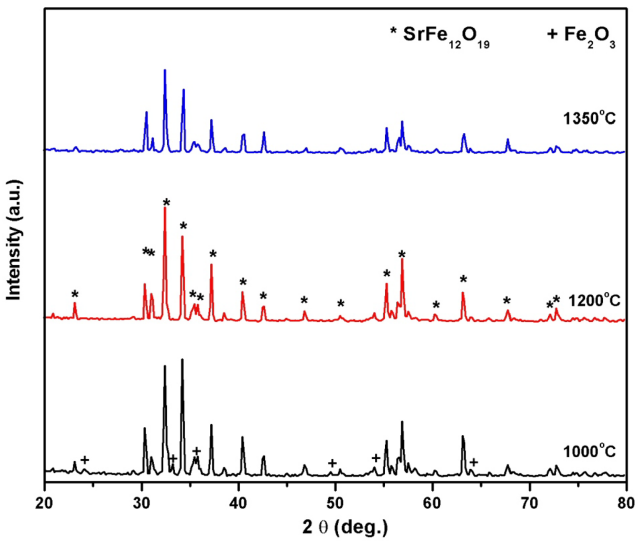

Fig. 5. (Color online) XRD patterns of $SrFe_{12}O_{19}$ for Sr^{2+}:Fe^{3+} molar ratio 1.3:12 treated at different temperatures.

the crystallite size of $SrFe_{12}O_{19}$ was found to increase. Table 2 shows that the crystallite size was increased from 111 to 143 nm with an additional increase in annealing temperature from 1000 to 1350 °C for a 1:12 molar ratio of Sr^{2+} to Fe^{3+}. At the same time, with the similar mentioned temperatures, the Sr^{2+}:Fe^{3+} molar ratio was increased by 1.1:12 while the crystallite size was increased from 123.8 to 172.7 nm. Similarly, with that mentioned temperatures (1000-1350 ^{o}C), there was an increase in the crystallite size from 124.1 to 163.6 nm and from 121.5 to 147.9 nm with extra increasing Sr:Fe molar ratio of 1.2:12 and 1.3:12, respectively. Notably, these findings plainly show that the Sr^{2+}:Fe^{3+} molar ratio had an impact on crystallite size. Due to the contribution of impurities phases observed at lower and higher Sr:Fe molar ratios, pure and single-phase $SrFe_{12}O_{19}$ formed at a molecular ratio of Sr^{2+}:Fe^{3+}. The crystallite size at 1.1:12 is bigger than that seen at both lower and higher Sr^{2+}:Fe^{3+} molar ratios. Furthermore, the grain growth and the reduction of internal stress were the causes of the increase of the crystallite size with an increase in annealing temperature.

Crystalline materials have important features, which are lattice parameters to identify and reveal their structural properties. Recently, the ability to reduce experimental temporal cost and expenses of determination of lattice parameters through computational approaches has gained significant importance. The variation of lattice parameters and unit cell volume of $SrFe_{12}O_{19}$ powder as a function of annealing temperature and Sr^{2+}:Fe^{3+} mole ratio are shown in Table 3. Therefore, it is noticeable from the results that annealing temperature strongly affects the lattice parameters; however, it has negligible effects on unit cell volume. Additionally, Table 2 demonstrates that the lattice constants of the annealed hexagonal ferrite particles increased due to the presence of α-Fe_2O_3 and impurities. Likewise, with increasing the annealing temperature and as a result of the formation of M-type hexaferrite, lattice constants were found to be decreased. Furthermore, to determine the structure type, an examination of the aspect ratio *c*/*a* can be used [12, 14, 37, 38]. The M-type (magnetoplumbite) structure can be anticipated if the ratio is found to be between 3.917 and 3.963. The *c*/*a* ratios of the as-prepared samples (3.911-3.920) are also clearly within the range of M-type structures, as seen in Table 2.

Table 2. Crystallite size, lattice parameters, and unit cell volume of $SrFe_{12}O_{19}$ nanocrystalline for different Sr^{2+}:Fe^{3+} mole ratios.

Composition	Annealing temperature ^{o}C	Crystal size (nm)	Lattice parameter (Å)			Volume (Å)
			a	c	c/a	
1:12	1000	111	5.8725	22.9863	3.91421	686.514
	1200	134	5.8718	22.9954	3.91825	686.627
	1350	143	5.8628	22.9952	3.91388	685.895
1.1:12	1000	123.8	5.8666	22.9938	3.91947	685.345
	1100	146.8	5.8733	22.9770	3.91209	686.421
	1200	162.6	5.8738	22.9734	3.91115	686.441
	1350	172.7	5.8745	22.998	3.91485	687.335
1.2:12	900	126.5	5.8779	23.0151	3.91554	688.629
	1000	124.1	5.8664	22.9791	3.91706	684.273
	1100	140.3	5.8670	22.9627	3.91390	684.511
	1200	153.4	5.8795	22.9532	3.9139	687.149
	1300	160.4	5.8693	22.9906	3.91710	685.983
	1350	163.6	5.8685	23.0042	3.91991	686.115
1.3:12	1000	121.5	5.8683	23.0086	3.92083	686.186
	1200	134.6	5.8792	23.0173	3.91506	688.994
	1350	147.9	5.8736	23.0094	3.91742	687.4614

Table 3. Spot analysis average of constituent elements in the $SrFe_{12}O_{19}$ phase, wt.%.

Element	Sr		Fe		O	
	Mass%	Atom%	Mass%	Atom%	Mass%	Atom%
EDX1	9.38	3.31	56.96	31.57	33.65	65.11
EDX2	9.54	3.41	57.60	32.29	32.86	64.30

3.2. Microstructure Characterization

SEM analysis was carried out for further investigation to show the surface morphology of the synthesized hexaferrite and the development of grain structure. Moreover, different representative areas with different magnifications were taken to show the most important microstructures and phenomena. SEM micrographs produced Sr–M-type hexaferrite $SrFe_{12}O_{19}$ at Sr^{2+}:Fe^{3+} molar ratios 1:12 for annealing temperatures from 1000 to 1350 °C were displayed in Fig. 6. Similar to this, Fig. 6(a, b) depicts fine precipitated particles with a wide particle size distribution, random grain orientation, and growing hexagonal platelet structures. It can be inferred that given that temperature, single-phase strontium hexaferrite was not able to develop. In addition to that, with a further increase in temperature, the grains started to grow again. As the annealing temperature rose to 1200 °C, it can be seen from Fig. 6(c, d) that the formed M-hexaferrite powders had a hexagonal plate-like structure and contained fewer cubic small particles. A comparable trend has also emerged for the sample that was annealed at 1350 °C, as shown by Fig. 6(e, f). Besides, a multilayer of hexagonal platelet-like structure was observed, and more crystal growth occurred with a uniform coarse structure. Additional characteristics of the microstructures of the particles created at higher Sr^{2+}:Fe^{3+} molar ratios of 1.1:12, 1.2:12, and 1.3:12, respectively, at different temperatures are shown in Figs. 7-9. Noticeably, as presented in the a and b sites of Figs. 7-9, uncertain morphology, which showed up in all instances as fine particles with a wide distribution and various shapes for the sample annealed at 1000 °C. Although, at an annealing temperature ≥ 1000 °C, a well-crystalline homogeneous hexagonal platelet-like structure appeared. Additionally, it is revealed that the grain of the hexagonal platelet structure was enhanced with a further increase in the annealing temperature to 1350 °C.

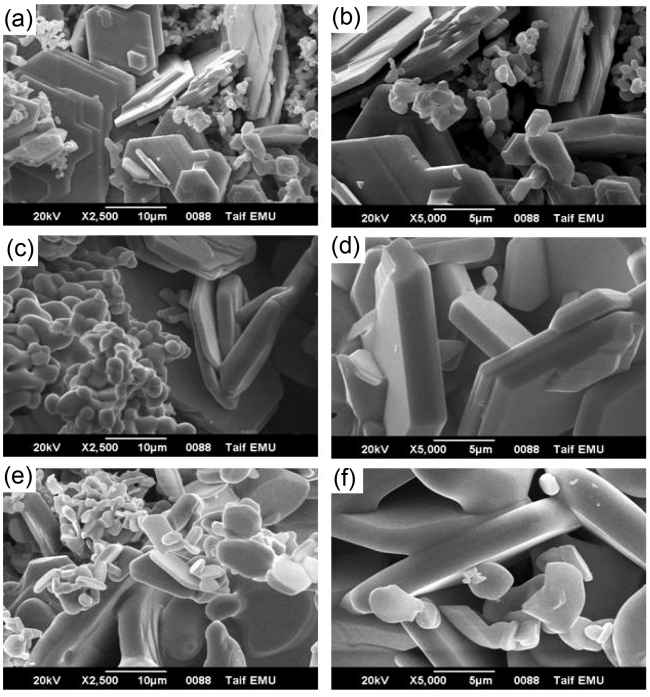

Fig. 6. SEM micrographs of $SrFe_{12}O_{19}$ nanopowders for Sr^{2+}:Fe^{3+} molar ratio 1:12 with different temperatures: (a, b) 1000 °C, (c, d) 1200 °C, and (e, f) 1350 °C.

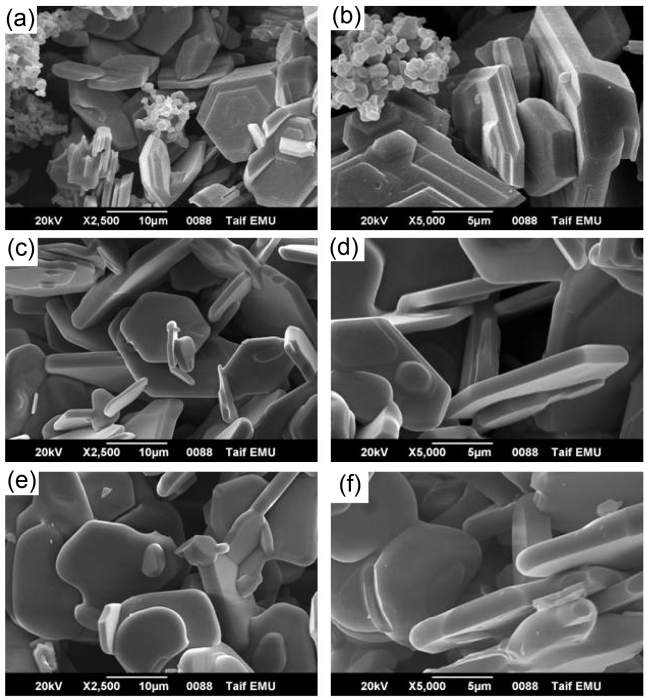

Fig. 7. SEM micrographs of $SrFe_{12}O_{19}$ nanopowders for Sr^{2+}:Fe^{3+} molar ratio 1.1:12 with different temperatures: (a, b) 1000 °C; (c, d) 1200 °C; (e, f) 1350 °C.

To clarify the distribution of each element in the structure, making maps for each constituent element used qualitative analysis for the different elements in the $SrFe_{12}O_{19}$ nanopowders sample. Fig. 10 presents the SEM mappings of strontium hexaferrite obtained at 1100 °C and Sr^{2+}:Fe^{3+} molar ratio 1.1:12. This presentation is in relation to the distribution of strontium, iron, and oxygen, which is shown in Fig. 10(b), 10(c) and 10(d), respectively. Moreover, Fig. 10(e, f) demonstrated the energy dispersive X-ray spectra (EDX). These maps indicate that the distributions of the three elements were almost the same. This also signifies a good homogenous microstructure for the prepared hexaferrite powders. Table 3 displays the element distribution of strontium (≈ 3.4%), iron (≈ 32%), and oxygen (≈ 65%) via the EDX spot

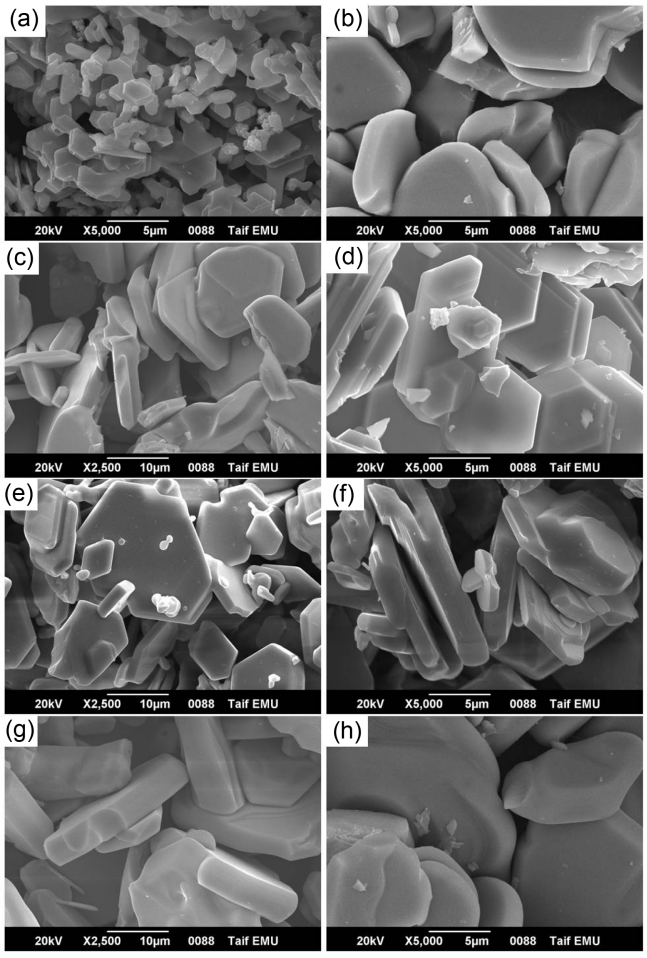

Fig. 8. SEM micrographs of $SrFe_{12}O_{19}$ nanopowders for Sr^{2+}:Fe^{3+} molar ratio 1.2:12 with different temperatures: (a) 900 ºC; (b) 1000 ºC; (c, d) 1100 ºC; (e, f) 1200 ºC; (g, h) 1350 ºC.

analysis of $SrFe_{12}O_{19}$ hexaferrites at 1100 °C.

3.3. Magnetic Properties of Synthesized $SrFe_{12}O_{19}$

The magnetic hysteresis loops (*M-H* curves), produced using tartaric acid as a fuel and obtained at various temperatures (1000-1350 ºC), are shown in Figs. 11-14. They were measured by VSM at room temperature with a maximal applied field of 20 kOe. Table 4 provides examples of the magnetic characteristics, including saturation magnetization (M_s), residual magnetization (M_r), squareness ratio (M_r/M_s), and coercivity field (H_c).

As a disclosure, the results of the magnetic properties of particles showed high reliance upon the annealing temperature adopted. Fig. 11 (Sr^{2+}:Fe^{3+} Molar ratio 1.1:12) shows that M_s was found to gradually increase and reach 55.5 maximum values at 1350 °C. The coercive force H_c reached its optimum of 685.5 Oe at the same temperature (1350 °C). Remarkably, it is understandable that the

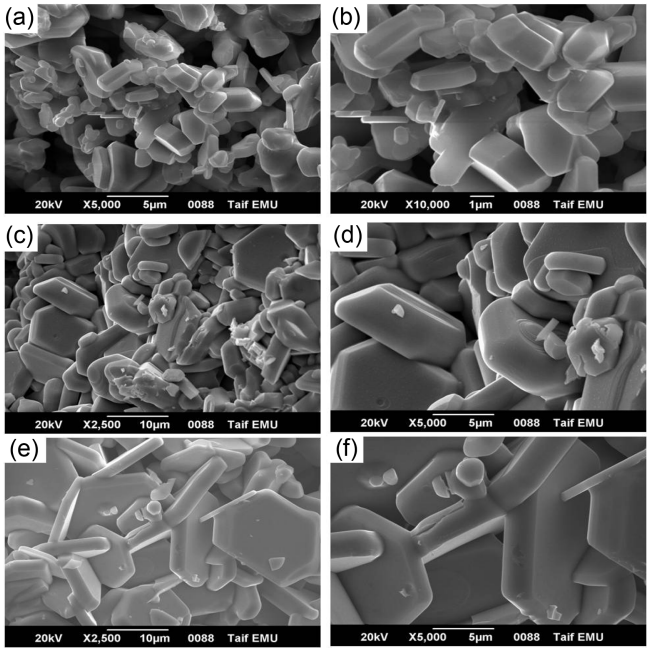

Fig. 9. SEM micrographs of $SrFe_{12}O_{19}$ nanopowders for Sr^{2+}:Fe^{3+} molar ratio 1.3:12 with different temperatures: (a, b) 100 ºC; (c, d) 1200 ºC; (e, f) 1350 ºC.

composition of crystal phases and the growth of crystallites are extremely affecting the evolution behaviors of M_s, M_r, and H_c. Furthermore, the formation of large amounts of intermediate α-Fe_2O_3, as the XRD analysis shows, and the low crystallinity of $SrFe_{12}O_{19}$ are the valid reasons for the appearance of the lower M_s and H_c at the Sr^{2+}:Fe^{3+} molar ratio of 1:12. Moreover, the saturation magnetization M_s of the powders shows a consistent rise when the annealing temperature hit a maximum of 55.5 emu/g. This improvement in M-type ferrite crystallinity and phase homogeneity with raising the annealing temperature may cause the M_s to rise with temperature.

Fig. 12 provides a detailed explanation of the magnetic characteristics of strontium M-type hexaferrite made at various annealing temperatures using a Sr^{2+}:Fe^{3+} molar ratio of 1.1:12. Similarly, the rise in $SrFe_{12}O_{19}$ phase evolution and grain size with higher annealing temperatures was correlated with an increase in saturation magnetization (M_s) and remanence (M_r). The highest saturation magnetization (M_s = 65.3 emu/g) was attained after two hours of annealing at 1350 ºC. Otherwise, the high coercive force (1180.2 Oe) can be attained at 1350 ºC. However, the values of the coercive field were lower than those obtained via the coprecipitation route [24]. This low coercive field makes them ideal for microwave devices, security, switching, and sensing applications. Producing such low fields with small permanent magnets or low-

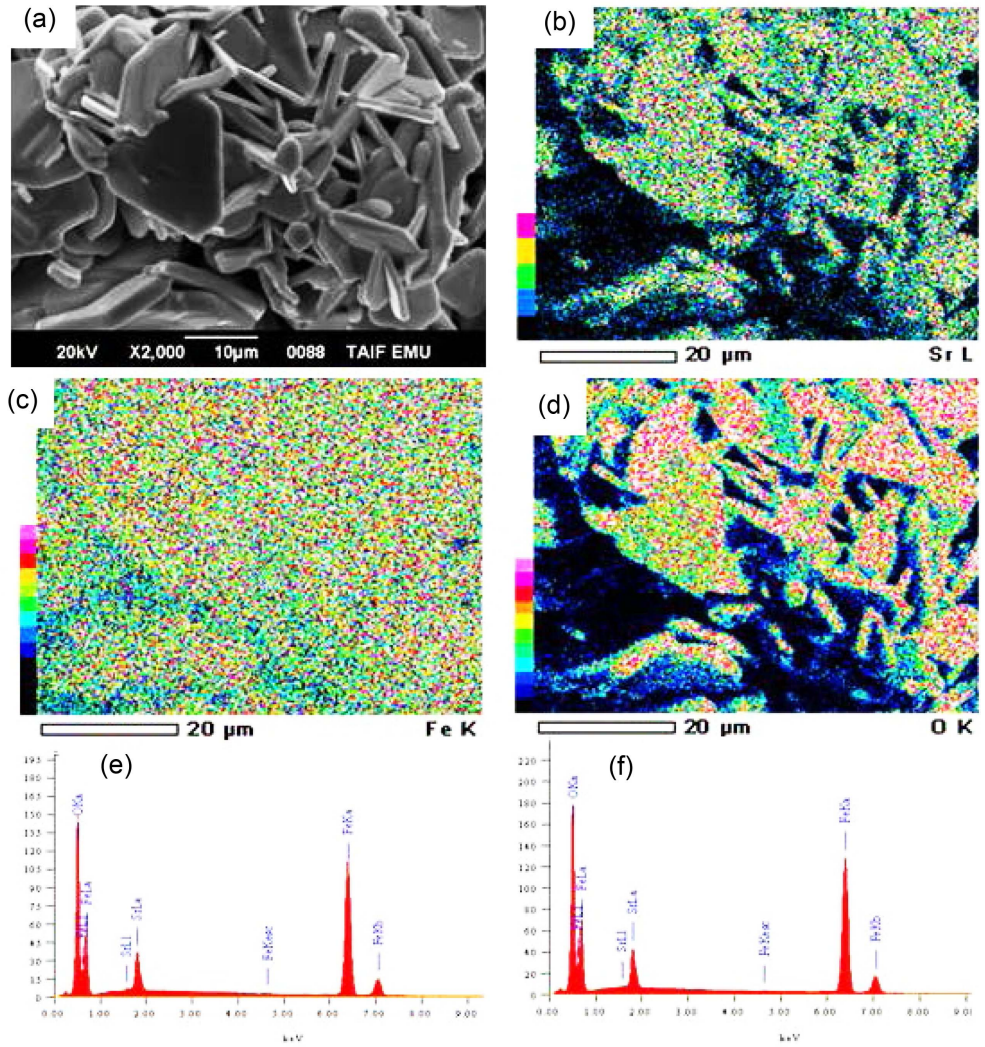

Fig. 10. (Color online) The SEM mappings of $SrFe_{12}O_{19}$ obtained at 1100 °C and Sr^{2+}:Fe^{3+} molar ratio 1.1:12 for the distribution of (a) real image, (b) strontium, (c) iron, (d) oxygen, and (e & f) the associated EDX spectra

power electromagnets is simple. Additionally, it has been noted that one of the requirements for EM materials is coercivity with values up to a few hundred oersteds, making these materials ideal for the suppression of EMI and microwave devices [36]. High structural and chemical stability, high saturation magnetization, and cheap cost are also notable criteria for most recording media. High coercivities are avoided for recording material using hard disks, floppy disks, and videotape to make re-recording easier. High coercivity is required for recording materials used in identity cards and credit cards to minimize the chance of data corruption when the cards are exposed to errant magnetic fields.

Fig. 13 clearly illustrates the M-H hysteresis loops of hexagonal ferrite powders with a Sr^{2+}:Fe^{3+} molar ratio of 1.2:12 at different temperatures. Similarly, increasing the annealing temperature to 1300 ºC led to a rise in saturation magnetization. However, the values were slightly higher than that obtained at the Sr^{2+}:Fe^{3+} molar ratio of 1.1:12. Maximum saturation magnetization (M_s = 66.2 emu/g) was accomplished at an annealing temperature of 1300 ºC, while the highest coercive force (1215.3 Oe) can be attained at 1200 ºC. Both the increase in saturation magnetization (M_s) and the increase in coercivity (H_c) were related to the presence of well-crystalline, moderately high crystallinity $SrFe_{12}O_{19}$ powders. Changing the Sr^{2+}:Fe^{3+} molar ratio to 1.3:12 (Fig. 14) decreased the saturation magnetization compared to that obtained at Sr^{2+}:Fe^{3+} molar ratio 1.2:12. This is due to the increase of the presence of nonmagnetic species of Fe_2O_3 as observed from the XRD results. The coercive force H_c of the $SrFe_{12}O_{19}$ specimen highly increased at Sr^{2+}:Fe^{3+} molar

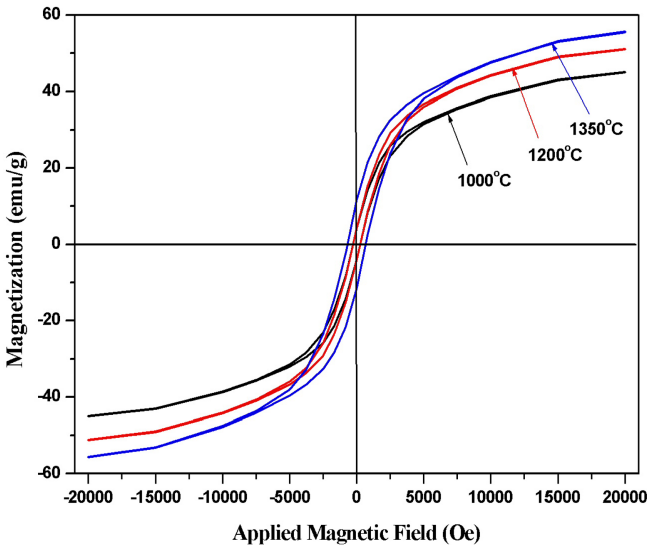

Fig. 11. (Color online) *M-H* loop*s* of $SrFe_{12}O_{19}$ powders for Sr^{2+}:Fe^{3+} molar ratio 1:12 with different annealing temperatures.

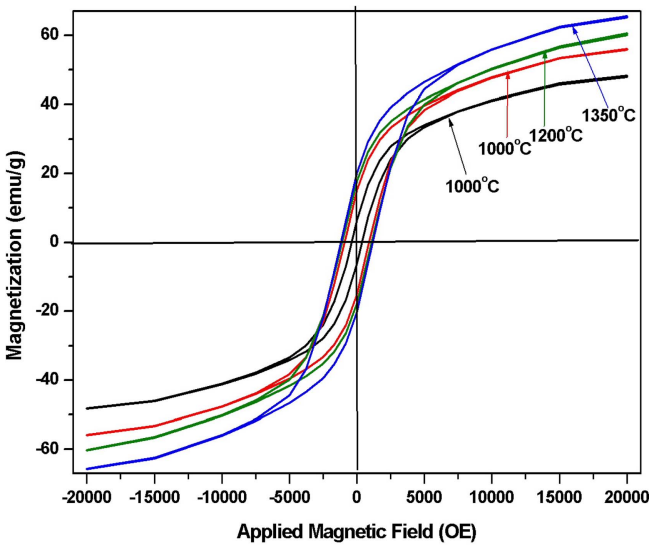

Fig. 12. (Color online) *M-H* loop*s* of $SrFe_{12}O_{19}$ powders for Sr^{2+}:Fe^{3+} molar ratio 1.1:12 with different annealing temperatures.

ratio into 1.3:12. Maximum coercive force H_c (2107.8 Oe) was obtained at an annealing temperature of 1000 ºC and decreased with the increase of temperature. These results might be related to the residual α-Fe_2O_3 having a high intrinsic coercive force and the change of the crystalline size of $SrFe_{12}O_{19}$ and α-Fe_2O_3 phases. It is reported that the change in coercive force was related to the change in the particle size due to annealing, the change in microstructure, and the presence of residual of α-Fe_2O_3 [39].

The squareness of the hysteresis loop can be measured essentially from the squareness ratio M_r/M_s (Stoner-Wohlfarth value) [40], which are important for synthesizing nanocrystalline magnetic materials. The M_r/M_s ratio

Table 4. Magnetic properties of $SrFe_{12}O_{19}$ powders for different Sr^{2+}:Fe^{3+} molar ratios.

Composition Sr:Fe	Temperature (ºC)	Magnetic properties			
		Saturation magnetization M_s (emu/g)	Retentivity M_r (emu/g)	Coercivity H_c (Oe)	M_r/M_s
1:12	1000	45.016	4.905	275.09	0.109
	1200	51.13	5.5438	420.3	0.108
	1350	55.502	8.281	685.46	0.221
1.1:12	1000	47.973	5.56	389.28	0.116
	1100	55.866	11.8	916.85	0.211
	1200	60.066	16.04	1100	0.267
	1350	65.283	18.42	1180.2	0.282
1.2:12	900	37.26	4.89	420.83	0.131
	1000	48.69	10.32	352.69	0.212
	1100	54.59	13.02	794.74	0.238
	1200	61.11	15.153	1215.3	0.248
	1300	66.19	25.54	1131.9	0.386
	1350	63.25	24.01	1120.1	0.380
1.3:12	1000	53.97	14.67	2107.8	0.272
	1200	55.44	22.05	1682.3	0.398
	1350	60.45	24.68	940	0.408

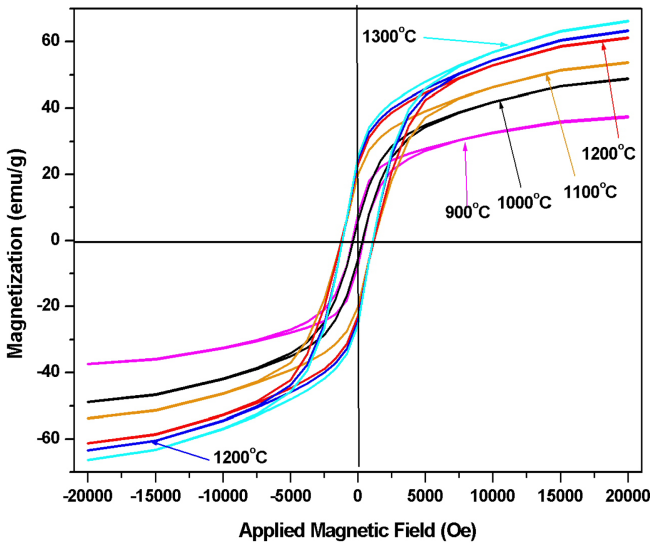

Fig. 13. (Color online) *M-H* loop*s* of $SrFe_{12}O_{19}$ powders for Sr^{2+}:Fe^{3+} molar ratio 1.2:12 with different annealing temperatures.

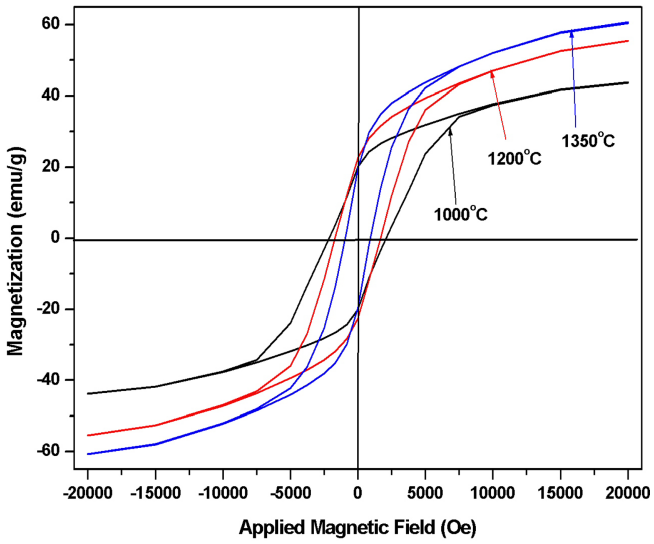

Fig. 14. (Color online) *M-H* loop*s* of $SrFe_{12}O_{19}$ powders for Sr^{2+}:Fe^{3+} molar ratio 1.3:12 with different annealing temperatures.

extracted from hysteresis loops showed that M_r/M_s increased with increasing annealing temperature for all samples. Moreover, the M_r/M_s value increased with increasing Sr^{2+}:Fe^{3+} molar ratio. Maximum M_r/M_s (≈0.408) was observed at 1350 °C for a sample with Sr^{2+}:Fe^{3+} molar ratio 1.3:12. However, the squareness ratio (M_r/M_s) is found to be very small and < 0.5 for all studied samples. These values are expected for hexaferrite in multimagnetic domains. It is reported that if the squareness ratio (M_r/M_s) ≤ 0.5, then the hexaferrites are in multimagnetic domains; while if the squareness ratio (M_r/M_s) ≥ 0.5, then the hexaferrites are in single domain [41].

4. Conclusion

M-type $SrFe_{12}O_{19}$ nanocrystalline powders were fabricated using the simple self-combustion tartrate precursor approach at relatively low annealing temperatures. The annealing temperature and Sr^{2+}:Fe^{3+} molar ratio play a substantial role in the fabrication of $SrFe_{12}O_{19}$ nanocrystalline powders using the tartaric acid precursor strategy. Single-phase Sr-hexagonal ferrite could not be obtained at a Sr^{2+}:Fe^{3+} mole ratio of 1:12 and contains impurity peaks of the α-Fe_2O_3 phase even after raising the annealing temperature to 1350 °C. Well-crystalline single-phase M-hexagonal ferrite was realized at a low annealing temperature of 1100 °C for 2 h at Sr^{2+}:Fe^{3+} concentrations of 1.1:12, 1.2:12, and 1.3:12. Pure single-phase $SrFe_{12}O_{19}$ formed at a Sr^{2+}:Fe^{3+} molar ratio of 1.1:12 has larger crystallite size than that observed at both lower and higher Sr^{2+}:Fe^{3+} molar ratio. The lattice parameters were found to increase with the existence of α-Fe_2O_3 and impurities in the annealed hexagonal ferrite powders, while they decrease with increasing the annealing temperature. The *c*/*a* ratios of as-prepared samples (~3.911-3.920) are well within the ratio range of M-type structures. The annealing temperature and the molar ratio of Sr^{2+} to Fe^{3+} had a significant impact on the microstructures of the produced particles. At an annealing temperature of 1000 °C, the well-crystalline uniform hexagonal platelet-like structure has emerged. The hexagonal platelet structure's grain was improved with a further rise in annealing temperature to 1350 °C. The SEM mappings and EDX spot analysis showed a good homogenous microstructure for the prepared hexaferrite powders. The saturation magnetization M_s and the coercive force H_c were found to gradually increase and reach maximum values at 1350 °C. At various synthesis circumstances, wide saturation magnetization M_s (37.26-66.19 emu/g) and coercivities (275.09-2107.8Oe) were attained.

References

[1] J. L. Snoek, Physica **14**, 207 (1948).
[2] S. Son, M. Taheri, E. Carpenter, V. G. Harris, and M. E. McHenry, J. Appl. Phys. **91**, 7589 (2002).
[3] R. Valenzuela, Phys. Res. Int. **2012**, 1 (2012).
[4] S. M. Rajaram, V. J. Vijaykumar, Micro and Nano Technologies. Elsevier 2020.
[5] A. K. Singh, M. G. H. Zaidi, P. L. Sah, and R. Saxena, European J. Adv. Eng. Technol. (EJAET0) **5**, 350 (2018).

[6] B. D. Cullity and C. D. Graham, John Wiley & Sons (2011).
[7] R. C. Pullar, Progress in Materials Science **57**, 1191 (2012).
[8] V. K. Chakradhary and M. J. Akhtar, Compos. B. Eng. **183**, 107667 (2020).
[9] M. Zareen, N. Yasmin, I. A. Malik, M. Zahid, M. N. Ashiq, A. Kiran, H. Javed, M. Safdar, and M. Mirza, J. Magn. Magn. Mater. **497**, 165943 (2020).
[10] M. Khandani, M. Yousefi, S. S. S. Afghahi, M. M. Amini, and M. Bikhof Torbati, Mater. Chem. Phys. **235**, 121722 (2019).
[11] G. Qi, Y. Liu, Y. Chen, Qian Liu, J. Chen, Q. Yin, and H. Zhang, J. Mater. Sci: Mater Electron (2020).
[12] M. M. Hessien, D. A. Rayan, M. H. H. Mahmoud, A. Alhadrami, and M. M. Rashad, J. Mater. Sci. Mater. Electron **29**, 9771 (2018).
[13] A. V. Trukhanov, S. V. Trukhanov, V. G. Kostishyn, L. V. Panina, V. V. Korovushkin, V. A. Turchenko, D. A. Vinnik, E. S. Yakovenko, V. V. Zagorodnii, V. L. Launetz, V. V. Oliynyk, T. I. Zubar, D. I. Tishkevich, and E. L. Trukhanova, J. Magn. Magn. Mater. **462**, 127 (2018).
[14] M. M. Hessien, N. El-Bagoury, M. H. H. Mahmoud, M. Alsawat, A. K. Alanazi, and M. M. Rashad, J. Magn. Magn. Mater. **498**, 166187 (2020).
[15] M. A. Almessiere, Y. Slimani, N. A. Tashkandi, A. Baykal, M. F. Saraç, A. V. Trukhanov, I. Ercan, I. Belenli, and B. Ozçelik, Ceram. Intern. **45**, 1691 (2019).
[16] M. M. Hessien, M. M. Rashad, M. S. Hassan, and K. El-Barawy, J. Alloys Compd. **476**, 3732 (2009).
[17] V. Turchenko, V. G. Kostishyn, S. Trukhanov, F. Damay, F. Porcher, M. Balasoiu, N. Lupu, B. Bozza, I. Fina, A. Trukhanov, J. Walisewski, K. Recko, and S. Polosan, J. Alloys Compd. **82**, 153412 (2020).
[18] V. Banihashemi, M. E. Ghazi, and I. Izadifard, J. Mater. Sci. Mater. Electron. **30**, 17374 (2019).
[19] M. A. Almessiere, Y. Slimani, S. Güner, J. van Leusen, A. Baykal, and P. Kögerler, Mater. Sci. Mater. Electron. **30**, 11181 (2019).
[20] T. S. Chin, J. Magn. Magn. Mater. **209**, 75 (2000).
[21] A. Cochardt, J. Appl. Phys. **34**, 1273 (1963).
[22] M. M. Hessien, M. Radwan, and M. M. Rashad, J. Anal. Appl. Pyrolysis **78**, 282 (2007).
[23] S. Garehbaghi and A. Kianvash, Results Phys. **12**, 1559 (2019).
[24] M. M. Hessien, M. M. Rashad, and K. El-Barawy, J. Magn. Magn. Mater. **320**, 336 (2008).
[25] A. Ataie and S. H. Manese, J. Eur. Ceram. Soc. **21**, 1951 (2001).
[26] F. Wang, C. B. Ponton, R. Grössinger, and I. R. Harris, J. Alloy. Compd. **369**, 170 (2004).
[27] A. Davoodi and B. Hashemi, J. Alloys Compd. **509**, 5893 (2011).
[28] C. Serletis, G. Litsardakis, E. Pavlidou, and K. G. Efthimiadis, Physica B Condens **525**, 78 (2017).
[29] S. Sugimoto, K. Haga, T. Kagotani, and K. Inomata, J. Magn. Magn. Mater. **290-291**, 1188 (2005).
[30] A. Kumar, R. K. Singh, H. K. Satyapal, Monalisa, A. Kumar, and S. Sharma, Physica B Condens **600**, 412592 (2021).
[31] Z. Wang, W. Yang, Z. Zhou, M. JIn, J. Xu, and Y. Sui, J. Supercond. Nov. Magn. **29**, 981 (2016).
[32] R. Müller, J. Magn. Magn. Mater. **120**, 61 (1993).
[33] R. Nikkhah-Moshaie, A. Ataie, and S. A. Seyyed Ebrahimi, J. Alloys Compd. **429**, 324 (2007).
[34] P. Sharma, R. A. Rocha, and A. Paesano Jr, J. Alloys Compd. **443**, 37 (2007).
[35] P. N. Anantharamaiah, N. S. Chandra, H. M. Shashanka , R. Kumar, and B. Sahoo, Adv Powder Technol. **31**, 2385 (2020).
[36] M. Jang, M. S. Chang, Y. Kwon, S. Yang, J. Gwak, S. J. Kwon, J. Lee, K. Song, C. R. Park, S. B. Lee, B. Park, and J. W. Jeong, Nanoscale **13**, 12004 (2021).
[37] V. O. Turchenko, A. V. Trukhanov, I. A. Bobrikov, S. V. Trukhanov, and A. M. Balagurov, Journal of Surface Investigation: X-ray, Synchrotron and Neutron Techniques **1**, 17 (2015).
[38] V. O. Turchenko, A. V. Trukhanov, I. A. Bobrikov, S. V. Trukhanov, and A. M. Balagurov, Crystallography Reports **60**, 629 (2015).
[39] Y.-P. Fu and C.-H. Lin, J. Alloys Compd. **386**, 222 (2005).
[40] E. C. Stoner and E. P. Wohlfarth, The R. Soc. Lond. A **240**, 599 (1948).
[41] M. N. Ashiq, R. B. Qureshi, M. A. Malana, and M. F. Ehsan, J. Alloys Compd. **617**, 437 (2014).